AMERICAN ACADEMY OF OPHTHALMOLOGY®

Impact of Elevated Intraocular Pressure on Lamina Cribrosa Oxygenation: A Combined Experimental–Computational Study on Monkeys

Yuankai Lu, PhD,[1] *Yi Hua, PhD,*[1,2,3] *Bingrui Wang, PhD,*[1] *Qi Tian,*[4] *Fuqiang Zhong, PhD,*[1] *Andrew Theophanous,*[4] *Shaharoz Tahir,*[4] *Po-Yi Lee, PhD,*[1,4] *Ian A. Sigal, PhD*[1,4]

Purpose: To evaluate how lamina cribrosa (LC) oxygenation is affected by tissue distortions resulting from elevated intraocular pressure (IOP).

Design: Experimental study on 4 monkeys, histology, and computational analysis.

Subjects: Four healthy monkey eyes with OCT scans at IOPs of 10 to 60 mmHg.

Methods: Intraocular pressure–induced LC tissue deformations of a healthy monkey were measured in vivo using OCT images and digital volume correlation analysis techniques. Three-dimensional eye-specific models of the LC vasculature of 4 healthy monkey eyes were reconstructed using histology. The models were then used to compute LC oxygenation, first as reconstructed (baseline), and then with the LC vessels distorted according to the OCT-derived deformations. Two biomechanics-based mapping techniques were evaluated: cross-sectional and isotropic. The hemodynamics and oxygenations of the 4 LC vessel networks were evaluated at IOPs up to 60 mmHg to quantify the effects of IOP on LC oxygen supply, assorting the extent of LC tissue mild and severe hypoxia.

Main Outcome Measures: Intraocular pressure–induced deformation, vasculature structure, blood supply, and LC oxygenation.

Results: Intraocular pressure–induced deformations reduced LC oxygenation significantly and substantially. More than 20% of LC tissue suffered from mild hypoxia when IOP reached 30 mmHg. Extreme IOP (>50 mmHg) led to large severe hypoxia regions (>30%) in the isotropic mapping cases.

Conclusions: Our calculations predicted that moderately elevated IOP can lead to mild hypoxia in a substantial part of the LC, which, if sustained chronically, may contribute to neural tissue damage. For extreme IOP elevations, severe hypoxia was predicted, which would likely cause more immediate damage. Our findings suggest that despite the remarkable LC vascular robustness, IOP-induced distortions can potentially contribute to glaucomatous neuropathy.

Financial Disclosure(s): The author(s) have no proprietary or commercial interest in any materials discussed in this article.

Supplemental material available at www.ophthalmologyscience.org.

Vision loss in glaucoma is due to the loss of the retinal ganglion cells that transmit visual information to the brain.[1,2] Glaucomatous axonal damage is believed to initiate within the lamina cribrosa (LC) region of the optic nerve head (ONH), where the axons exit the globe.[1–5] Although neural tissue damage can occur even at normal levels of intraocular pressure (IOP), elevated IOP is a major risk factor for glaucoma, and currently, every method to prevent or treat glaucoma is based on reducing IOP.[6,7] Nevertheless, the mechanisms by which elevated IOP contributes to the neuropathy remain unclear, complicating the development of new improved methods to prevent vision loss.[8–14] A leading theory suggests that elevated IOP causes distortions of the ONH vasculature, particularly of the LC.[8,10,15–17] The distorted vessels have reduced blood flow within, resulting in compromised perfusion and, most importantly, reduced oxygenation of the neural tissues of the LC.[10,18,19] Even mild reductions in oxygenation, if sustained, can result in or contribute to neural tissue damage.[20–23]

Despite remarkable advances in the experimental techniques available to study ocular biomechanics and blood flow, obtaining detailed maps of the LC flow and oxygenation remains out of reach. Available techniques suffer, for example, from limited penetration (OCT and related light-based techniques)[24–28] or insufficient spatial or temporal resolutions (ultrasound and magnetic resonance

https://doi.org/10.1016/j.xops.2025.100725
ISSN 2666-9145/25

imaging[29,30]). Also importantly, several of these techniques are primarily aimed at detecting blood flow. While blood flow is important, studies note that it is crucial to measure and understand oxygenation.[27] Oxygenation is related to, but not identical to, blood flow. Techniques for measuring oxygenation within the blood vessels have been developed,[27] but application in deep vessels within the LC remains out of reach. Because of the experimental challenges, several groups have turned to theoretical[18,31] and computational modeling[9,10,32] to study LC hemodynamics and oxygenation and get a better understanding of the role of IOP-induced deformations. Theoretical models are particularly elegant, but they are only able to account for highly simplified anatomies and thus are not yet useful to analyze the extremely complex nature of eye-specific vascular networks. Computational models have been able to overcome this limitation, first using 2-dimensional models and later 3-dimensional (3D) flat LC anatomies.[9,10,18,33,34]

A 3D poroelastic model[33] was developed to simultaneously address LC hemodynamics and biomechanics. Another mathematical modeling work[10] employed a 2-dimensional generic LC model to simulate LC hemodynamics and oxygenation. In contrast, our model focuses specifically on the LC region using a 3D, eye-specific vascular network, enabling more detailed and realistic simulations of blood supply and oxygenation within the LC. Multiscale models[35] were developed to explore the hemodynamics and biomechanics for the entire eye. These models are important because they consider eye circulation as an integrated system, highlighting the interactions between biomechanics and hemodynamics across different regions in ocular pathology. The autoregulation mechanisms in the eye were incorporated into these models, supported by clinical results.[36]

We have developed a technique to reconstruct eye-specific models of the complex 3D vascular network of the LC region[37] and then use it for hemodynamics and oxygenation simulation.[32] Recently, we leveraged these techniques to study a set of eye-specific vascular networks and evaluate the effects of IOP-related tissue distortion on LC hemodynamics and oxygenation. We found that LC blood flow was sensitive to IOP-related vessel collapse, particularly if the collapses were clustered. An important finding was that normal local flow did not imply adequate oxygenation. In the study, however, we made several strong assumptions that we now aim to revisit in this work. For instance, as a first approximation, we considered the vessels as either open and unaffected by IOP or fully collapsed and closed. A better understanding of how IOP influences the LC, including blood flow and oxygenation, requires a more precise and subtle consideration of how IOP distorts vessels, the flow within, and from these the tissue oxygenation.

Our goal in this study was to improve the understanding of how LC oxygenation is affected by tissue deformations resulting from elevated IOP. We consider 4 eye-specific vascular networks from monkey ONHs. We analyzed the hemodynamics and oxygenation in the reconstructed baseline model, and then when subjected to experimentally derived IOP-induced tissue deformations. Compared with our previous report, herein we use a more refined approach to map experimental tissue deformations into vessel deformations, which then alter LC oxygenation. Also, because of the simplistic assumption of how blood vessels were affected by IOP (open or closed) in our previous study, we were unable to evaluate details of the effects of IOP and we only considered baseline and high IOPs (10 mmHg and 40 mmHg). Herein, we used a much more realistic approach to estimate vessel deformations with IOP and were thus able to also obtain a more refined understanding of tissue distortions and their effects.

Methods

General Procedure

We reconstructed 3D models of the LC vessel networks of 4 healthy monkey eyes from histological sections following previously reported techniques.[32,37,38] In vivo IOP-related tissue deformations within the LC were determined from a healthy monkey using OCT imaging and analysis techniques under controlled IOP conditions.[39] Two biomechanics-based techniques were then used to map the OCT-derived tissue strains to local LC to estimate their deformations. Lamina cribrosa hemodynamics and oxygenations of the 4-vessel networks were simulated as reconstructed, at baseline, and under several levels of IOP elevation (Fig 1). The outputs of these simulations were then analyzed to determine the effects of IOP on LC oxygenation (oxygen partial pressure [PO_2]). To interpret the results, the LC oxygen supply was classified into 3 levels based on the literature: normoxia (PO_2 >38 mmHg), mild hypoxia (38 mmHg greater than PO_2 >8 mmHg), and severe hypoxia (8 mmHg greater than PO_2). We subsequently provide more details of each of the steps.

Vascular Network Reconstruction

All procedures were approved by the University of Pittsburgh's Institutional Animal Care and Use Committee and adhered to both the guidelines set forth in the National Institute of Health's Guide for the Care and Use of Laboratory Animals and the Association for Research in Vision and Ophthalmology statement for the use of animals in ophthalmic and vision research. The reconstructions were made following the processes described elsewhere.[32,37] Briefly, 4 healthy female rhesus macaque monkeys' heads and necks were processed for vessel labeling. The anterior chamber of each eye was cannulated to control IOP throughout the experiment. Polyimide microcatheters were inserted into carotid arteries for vessel labeling, and the vascular bed was washed by warm phosphate-buffered saline to remove blood. A lipophilic carbocyanine dye, DiI, was used to label the vessels in the eye. We perfused 100 ml of the DiI solution into each carotid artery, followed by a phosphate-buffered saline wash, and then perfused 100 ml formalin into each carotid artery to fix the eye. Afterward, the eyes were enucleated, extraocular tissues were carefully removed, and immersion fixed in 10% formalin for 24 hours to complete fixation. We used formalin fixation because it

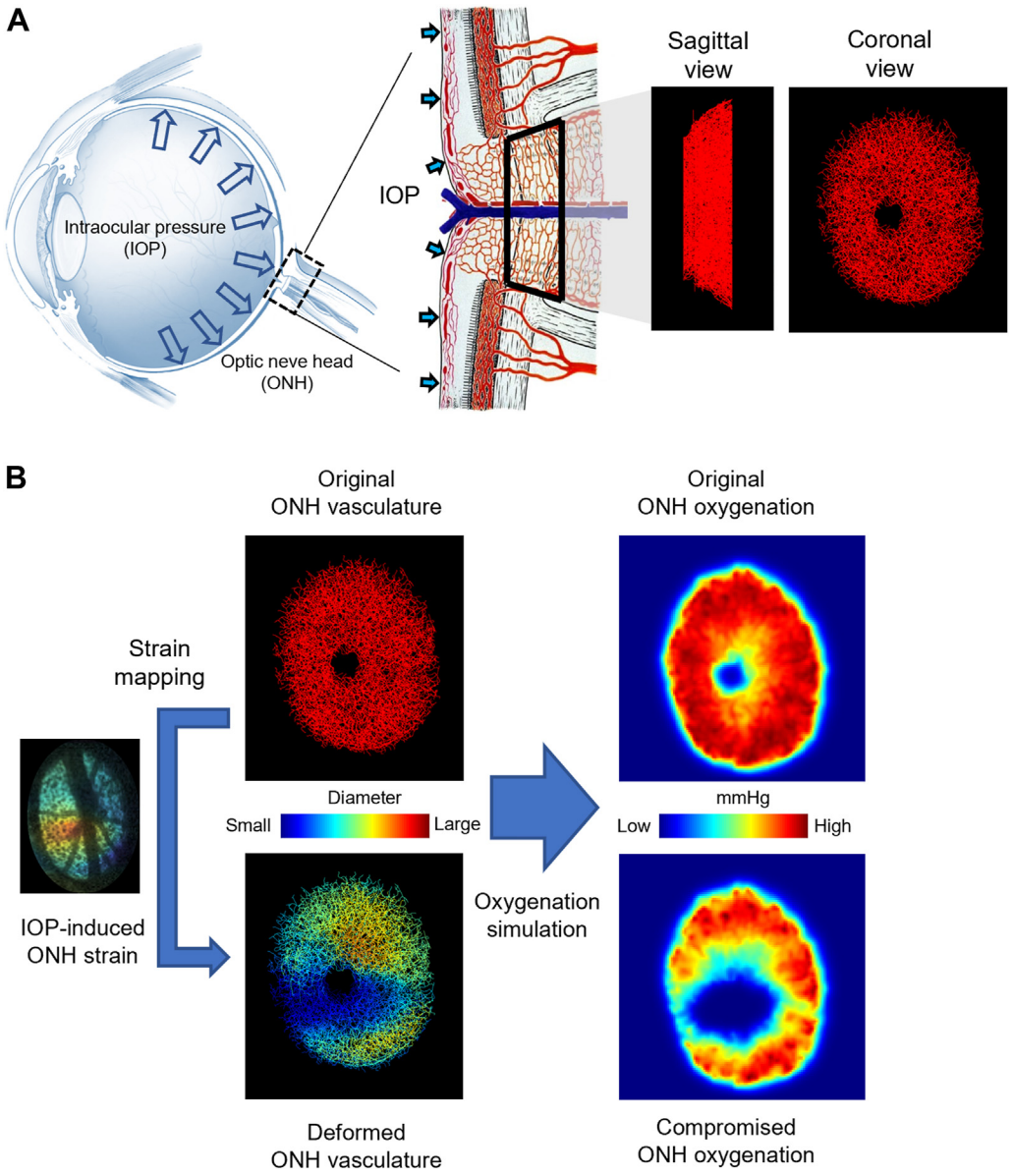

Figure 1. A, Diagrams of the eye and ONH vasculature (left and middle). An eye-specific model of ONH vasculature (right). The region reconstructed is indicated by the black trapezoid in the center panel. The region is part of the scleral canal, delimited at the periphery by the connective tissues of the sclera and pia mater, at the center by the central retinal artery and vein and by flat planes perpendicular to the central retinal artery and vein, at locations in the prelamina and retrolamina regions selected to ensure that the LC was completely enclosed. **B,** Schematic of our analysis process. The 4 eye-specific ONH vasculatures were reconstructed from histological sections, and their baseline hemodynamics and oxygenation were predicted by simulation. Experimental IOP-induced 3D deformation maps were then applied and used to predict vessel segment-specific distortions. The full LC hemodynamics and oxygenation were then recalculated for the networks with distorted vessels. The left-hand side of panel (**A**) was adapted from a diagram by the National Eye Institute. The middle panel was adapted from a classic drawing.[40] IOP = intraocular pressure; LC = lamina cribrosa; ONH = optic nerve head; 3D = 3-dimensional.

has been shown to only have a minimal effect on ocular tissues.[41]

The ONH and surrounding sclera were isolated using a 14-mm diameter trephine; the tissues were then cryoprotected and cryosectioned (16 μm thick) as described elsewhere.[32] Fluorescence microscopy and polarized light microscopy images were acquired to visualize vessels and collagen, respectively. Stacks of sequential fluorescence microscopy and polarized light microscopy images were aligned and registered in Avizo software (version 9.1). After registration, the fluorescence microscopy images were segmented and skeletonized to create a 3D reconstruction of the ONH vasculature.[37] Our reconstructed vascular networks included the whole LC region and some of the prelaminar and retrolaminar regions (Fig 1). This ensured that the 3D LC network was fully enclosed within the region reconstructed. Vessels in the LC region were identified based on the presence of

collagen beams in polarized light microscopy images. As in our previous work,[32] we could not ensure that the vessel diameters in the ex vivo sections were truly representative of the in vivo condition, and therefore, a uniform capillary diameter of 8 μm was assumed, as measured by An et al.[42]

Vascular Reconstruction Validation

To minimize clotting, which could prevent dye perfusion from reaching all vessel segments, we did our best effort to minimize the time between animal death and perfusion and extensively washed the ONH with phosphate-buffered saline. We estimate that all perfusions were started <90 minutes from death. Using a large dye volume ensured sufficient labeling. Fluorescence microscopy revealed strong signals in retinal and choroidal vessels, indicating successful perfusion. In some regions, signal was less strong, potentially due to partial occlusion of a vessel. However, these were still discernible by controlling the brightness and contrast settings.

Nevertheless, we acknowledge that there will always be some uneven labeling, discontinuities, or leaks that could impact the visualization and reconstruction. Manual intervention, including "cleaning" and "bridging" segments, was required. This could introduce potential artifacts and randomness in our final reconstructed model. To validate the reconstruction technique, we reconstructed the same eye twice by 2 individuals working independently from the same sections. We then processed both reconstructions using exactly the same steps to compute predictions of hemodynamics and oxygen distribution.

Vessel Deformation

The deformation of blood vessels is a classic biomechanical process, which is determined by many factors, including the surrounding tissue strain and stress environment, the compliance of the vessel wall, and luminal blood pressure.[43,44] In this work, we assumed that the small vessels of the ONH were primarily deformed by the in vivo ONH deformations (strain) resulting from an increase in IOP. While IOP was not directly included as a parameter in our biomechanical model, the IOP-induced tissue deformation was used for simulating vessel deformation. The deformations and corresponding changes on the flow are complex. To help readers discern changes, we prepared 5 supplementary videos. The videos illustrate blood flow (Videos 1, 4, and 5, available at www.ophthalmologyscience.org), vessel compression (Videos 2 and 5, available at www.ophthalmologyscience.org), and surrounding tissue oxygenation (Videos 3 and 5, available at www.ophthalmologyscience.org) for each vessel under varying IOP levels. Vessel compression is represented as the average cross-sectional compression for each vessel segment. Surrounding tissue oxygenation is defined as the average oxygenation of tissues within 20 μm of each vessel segment. This is the same general approach used elsewhere by us[45] and others.[10] This work, however, differs from previous ones in that we used a more refined biomechanics-based method to translate the in vivo ONH strains into local LC vessel deformations. Specifically, we performed in vivo OCT scans on a healthy monkey while IOP was controlled at 10 mmHg (baseline), 20 mmHg, 30 mmHg, 40 mmHg, 50 mmHg, and 60 mmHg. A digital volume correlation method was applied to measure the in vivo ONH strain from the OCT volumes, as reported before.[39] Since the in vivo ONH deformation and vascular networks are from different eyes, corresponding scaling and rotation were utilized to align the central retinal artery/vein and the temporal−nasal and superior−inferior axes. The approach was essentially the same as in a previous publication.[45] We then used a biomechanics-based technique to map the tissue strains to LC vessel distortions. These steps are described in more detail subsequently.

Deformation Mapping

To map the local strain tensor to the local vessel segment, we used an approach we call "cross-sectional strain mapping." This approach is based on modeling the blood vessels as hollow tubes embedded in the ONH, with the blood pressure applied on the vessel wall. This approach has the advantage that the deformation of ONH vasculature takes into consideration the complex network geometry, hemodynamics, and vessel−tissue interaction. A fully coupled model, however, is extremely complex and difficult to simulate. We therefore took advantage of some simplifications to approximate vessel deformation and evaluate the changes in blood flow and oxygenation. The flow resistance of vessels, crucial in determining vascular network hemodynamics, is highly sensitive to their diameters ($\propto d^{-4}$). As a result, we focused on the cross-sectional deformation of each vessel, as it closely relates to diameter variations.

Each vessel segment was assumed to be embedded in a tissue with a square cross-section, with the vessel centerline located at the center of the square (Fig 2). The entire region consisted of tissue and the hollow vessel lumen. Here, we assumed that the vessel wall had the same mechanical properties as the surrounding tissue. The boundary conditions of this system consist of the following: (1) the displacement boundary conditions on the side surface of the tissue region were interpolated from the in vivo ONH tissue deformation tensor and (2) the blood pressure boundary condition applied on the interior vessel wall was derived from the hemodynamic simulation. We applied a linear elastic model to simulate vessel wall deformation. The material properties were defined by a Young modulus of 0.3 MPa and a Poisson ratio of 0.5.[43] These parameters were incorporated into the governing equations to simulate the interaction between the tissue deformation and luminal blood pressure. Specifically, the deformation of the cross-section of the vessel satisfied the linear relationship:

$$\begin{bmatrix} (r_1 - r_0)/r_0 \\ (r_2 - r_0)/r_0 \end{bmatrix} = \begin{bmatrix} C_{11} & C_{21} \\ C_{12} & C_{22} \end{bmatrix} \begin{bmatrix} E_1 \\ E_2 \end{bmatrix} + C_P P$$

where r_1, r_2 were the semi-axes of the vessel cross-section, which was considered to be an ellipse under deformation, r_0 was the original radius of the vessel, E_1, E_2 were tissue strains added on the 2 in-plane principle directions, respectively, P was the luminal blood pressure (mmHg), and the coefficients C_{11}, C_{12}, C_{21}, C_{22}, and C_P were 3.03, 0.38, 0.38, 3.03, $5.9 \cdot 10^{-3}$, respectively. We

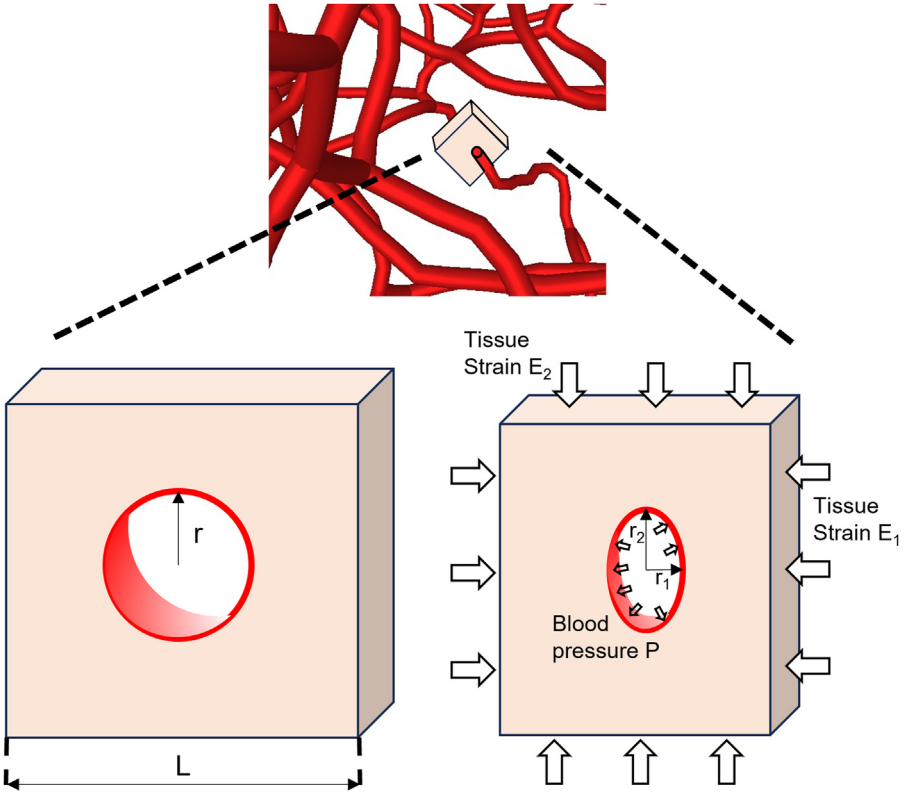

Figure 2. Diagram of the cross-sectional vessel deformation model. The vessel segment (red) was embedded in the center of the tissue (flesh color) with a square cross-section. The edge length L of the square was set to be 40 μm. The original radius (r) of the vessel was set to be 4 μm. The deformed vessel cross-section was considered as an ellipse with the semi-axes of r_1, r_2.

generated models with various parameters in Abaqus software and simulated vessel deformations. Multilinear fitting techniques were then applied to derive the coefficients from the simulation results.

Hemodynamic and Oxygenation Simulation

The hemodynamics of the 4 vascular networks were simulated at the baseline condition and subjected to IOP-induced deformations as described in the previous section. The vascular network was represented as a system of interconnected capillary elements. Considering the low Reynolds number in capillaries, the blood flow inside a cylinder-like capillary can be approximated by Poiseuille flow,

$$Q = \frac{\pi \Delta p}{8\mu L} r^4,$$

where Q is the blood flow rate, r is the vessel radius, L is the vessel length, μ is the blood viscosity, and Δp is the pressure drop along the vessel. The blood viscosity μ was described as a function of vessel radius and hematocrit (i.e., the volume fraction of red blood cells [RBCs]).[46,47] It is worth noting that both experimental observations and theoretical models reveal a dramatic increase in μ (viscosity) as the vessel diameter reaches the width of an RBC (~2 μm).[47] Namely, the vessel is nearly fully collapsed at that diameter. Flow and circulation of RBCs in tight vessels can be extremely complex. Such analysis is beyond the scope of this work, but interested readers are encouraged to read the papers by Pries and Secomb mentioned previously and by Ebrahimi and Bagchi.[48] A detailed description of the effective viscosity is provided in the supplemental materials.

When the vessel undergoes deformation due to IOP elevation, the cross-section of the vessel can be approximated as an ellipse, while the flow satisfies:[49]

$$Q = \frac{\pi \Delta p}{8\mu L} \frac{2(r_1 r_2)^3}{r_1^2 + r_2^2},$$

where the r_1, r_2 represent the axes of the ellipse cross-section of the vessel.

Pressure boundary conditions were applied to simulate the physiological blood supply for ONH. These were described and discussed in detail elsewhere.[45] Specifically, we divided the model boundaries into 4 surfaces for assigning the blood pressure conditions that irrigate the ONH region. The arteriole inlet pressure, representing blood inflow from the circle of Zinn−Haller, was set to 50 mmHg at the periphery. The central retinal vein, responsible for drainage, had a venule outlet pressure of 15 mmHg. The anterior ONH boundary and the posterior ONH boundary were set to pressures of 20 mmHg and 16 mmHg, respectively.

The oxygenation simulation for the ONH was based on the blood flow field, incorporating the modeling of oxygen transport from vascular networks to surrounding tissues. The physical principles of oxygen transport are well established,[50] including diffusion in the tissue and convection in the vessel. The governing equations for oxygen diffusion and consumption in tissue are:

$$D\alpha\Delta P = M(P), M(P) = M_0 P / (P_0 + P),$$

D and α are the oxygen diffusion coefficient and the oxygen solubility coefficient, respectively. Dα was treated as a single parameter in our models, and its value is listed in Table 1. P is the partial pressure of oxygen in tissues. The oxygen consumption rate $M(P)$ can be estimated by Michaelis−Menten enzyme kinetics, where M_0, P_0 are the Michaelis−Menten constants. In this study, M_0, which represents the demand of neural tissues, was assumed to be uniform throughout the ONH.

The oxygen flux in blood vessels satisfies:

$$f(P_b) = Q\left(H_D C_0 S(P_b) + \alpha_{\text{eff}} P_b\right)$$

where H_D represents the hematocrit, the RBC fraction within the blood flow, C_0 is the concentration of hemoglobin-bound oxygen in a fully saturated RBC, P_b is the blood oxygen concentration (mmHg), $S(P_b)$ is the oxygen−hemoglobin saturation as determined by the Hill equation, and α_{eff} is the effective solubility of oxygen in plasma. All parameters are listed in Table 1.

We used a fast and efficient method to simulate the convective and diffusive oxygen transport in the complex ONH vascular networks, as reported previously.[52] The comparison of oxygenation levels was analyzed between the baseline and deformed vessel networks to assess the impact of elevated IOP on the LC oxygenation.

Hypoxia Definition

We were interested in quantifying the effects of IOP on LC oxygenation. We therefore selected as an outcome measure the size of the region suffering hypoxia, or the "hypoxia region," as the way to quantify the LC oxygen supply to indicate potential damage from IOP elevation.

Tissue hypoxia, characterized by an insufficient supply of oxygen to tissues, often arises from structural and functional disturbance in the microcirculation.[23,53] Pathological processes driven by hypoxia involve complex biochemical mechanisms and vary significantly across different tissues.[21,23,54] A normal oxygen supply ensures physiological cellular activity, and a decrease in oxygenation increases the risk of damage to the tissues. When oxygen partial pressure declines to some critical levels, irreversible damage, such as tissue necrosis, can occur.[55] To distinguish the hypoxia level and the related potential tissue damage, we categorize tissues into 3 levels based on local oxygen partial pressure:

1. Normoxia (>38 mmHg): Normal cellular activity and metabolism.
2. Mild hypoxia (8−38 mmHg): Physiological responses to hypoxia occur. If sustained chronically, it may contribute to neural tissue damage.
3. Severe hypoxia (<8 mmHg): Tissue necrosis and irreversible damage at the short time scale.

We then assessed the volumetric fraction of these 3 types of regions. The mild and severe hypoxia regions are mainly used to evaluate the LC oxygenation challenge caused by elevated IOP. In our previous study on LC oxygenation, we provided a detailed rationale for our choices of oxygen tension levels.[45] Briefly, 8 mmHg (~1% oxygen) is a widely accepted threshold for severe hypoxia.[20,54–58] The threshold for normoxia, 38 mmHg (~5% oxygen), was chosen based on the literature.[55] Mild hypoxia is then defined as the intermediate state between normoxia and severe hypoxia. It is important to recall that this is not intended to suggest that there are no potentially ill effects of mild hypoxia. It seems plausible that the effects take longer or are more pronounced in tissues that are already in distress, for example, due to mechanical insult.

Alternative Approaches to Mapping the Compression:

As noted previously, there are currently no experimental methods suitable to measure IOP-induced distortions of the LC capillaries. Thus, it is necessary to define a way to map ONH strains to vessel segment distortions. Since this mapping directly determines the magnitude of the vessel distortions, it likely also plays a major role in the effects of IOP on the blood flow and oxygenation. While we still posit that the cross-sectional strain mapping technique described previously is reasonable, we are aware that the vessel distortion is complex and may depend on many other factors and mechanisms. Therefore, there could be other ways to assign vessel segment distortion from the tissue deformation. We were interested in exploring if other strain mapping techniques could lead to very different effects on the blood flow and oxygenation. To evaluate this, we decided to pick an alternative method that would represent a realistic worst-case limit. For this, we considered an approach in which each vessel segment experiences an isotropic compression from the surrounding tissues. In this case, the compression of the vessel radius was derived from the largest tissue compression, specifically, from the minimum eigenvalue of the strain tensor, E_3. We called this approach "isotropic compression mapping." In the isotropic case, the cross-sectional equation turns into

$$\frac{r - r_0}{r_0} = (C_{11} + C_{12})E_3 + C_P P$$

where r and r_0 are the compressed and original radius of the vessel, respectively. E_3 is the maximum tissue compression. We repeated the whole set of simulations, including every strain mapping and simulation, using this alternative mapping approach. The rationale was based on the lack of direct experimental evidence that the cross-

Table 1. Parameters Used in Hemodynamic and Oxygenation Simulations

Hemodynamic Parameters	Value	Reference
Vessel diameter	8 μm	32
Arteriole pressure	50 mmHg	32
Venule pressure	15 mmHg	32
Anterior blood pressure	20 mmHg	32
Posterior blood pressure	16 mmHg	32
Oxygenation parameters		
Oxygen diffusion coefficient, $D\alpha$	6×10^{-10} $mlO_2/cm/s/mmHg$	51
Effective oxygen solubility, α_{eff}	3.1×10^{-5} $mlO_2/ml/mmHg$	51
Consumption rate, M_0	5×10^{-4} $mlO_2/ml/s$	32
Oxygenation at half-maximal consumption, P_0	10.5 mmHg	51
Maximal RBC oxygen concentration C_0	0.5 mlO2/ml	51
Vessel deformation parameters		
Vessel compression parameter C_{11}, C_{22}	3.03	See text
Vessel compression parameter C_{12}, C_{21}	0.38	See text
Vessel compression parameter C_P	5.9×10^{-3}/mmHg	See text

RBC = red blood cell.

sectional mapping is accurate. In other words, we would anticipate that the actual effects of IOP would fall somewhere between the effects predicted using both approaches.

Results

Reconstruction Repeatability

The 2 vascular networks reconstructed independently from the same labeled eye exhibited extremely similar anatomy and oxygenation (Fig 3). Total vessel lengths were 547.68 mm and 528.68 mm, a difference of 3.3%. The average LC oxygen partial pressures were 55.56 mmHg and 54.85 mmHg, a difference of 1.3%. Altogether, this indicates excellent repeatability of our reconstruction process.

Four Eye-Specific Reconstructions

The 4 vascular networks used in our simulations are shown in Figure 4. The digital volume correlation–based ONH deformations are shown in Figure 5.

Effects of IOP-Induced Tissue Distortions

The effects of IOP increases on LC oxygenation using the cross-sectional approach are shown in Figures 6 to 8. The detailed vasculature deformation, hemodynamics, and oxygenation of eye 1 are shown in Figure 6 and Videos 1 to 3. At baseline, all vessel segments were assumed to be 8 μm in diameter. As IOP increased, tissue distortions led to decreased vasculature diameters and decreased ONH oxygenation. For briefness, we only show 1 eye. Similar patterns were observed in all 4 eyes. Although increased IOPs led consistently to vessel compressions, the changes in diameter of many vessels were not monotonic (Fig S9 and Video 2, available at www.ophthalmologyscience.org).

The LC oxygenation frequency distribution and the hypoxia region under various IOPs are shown in Figures 7 and 8. The IOP-induced deformations reduced LC oxygenation significantly in all the eyes ($P < 1e\text{-}5$). The effects of IOP were the largest with the IOP change from 10 to 20 mmHg. Further IOP increase had smaller effects per unit of IOP increase. The IOP elevation primarily contributed to the expansion of the mild hypoxia region, whereas the severe hypoxia region remained small (single digits %), even in cases of extremely high IOP. The effects of IOP varied between eyes (different panels in Fig 7 and different symbols in Fig 8), but the trends were similar.

As explained in the Methods section, we considered an alternative isotropic compression mapping method for mapping the digital volume correlation–measured deformations caused by IOP increases onto vessel distortions. The results were similar in distribution to those shown previously using the cross-sectional mapping method, except that the effects were larger. The most substantial difference was that vessel compression did result in a substantial region under severe hypoxia (<8 mmHg). The size of this region reached up to 40% at 60 mmHg in 1 eye. For briefness, these results are presented in supplemental material (Figs S10–S12, available at www.ophthalmologyscience.org).

Vessel Diameter Impact

To evaluate the impact of vessel diameter on LC oxygenation, we conducted additional simulations under 3 scenarios:

1. A 10% decrease in baseline diameter (7.2 μm) for each vessel.
2. A 10% increase in baseline diameter (8.8 μm) for each vessel.
3. Randomly distributed diameters between 7.2 and 8.8 μm for each vessel.

The above are baseline diameters before considering IOP-induced deformations. The results, presented in Figure 13, show that larger diameters yielded higher oxygenation levels and less hypoxic tissue. However, the overall trends in hypoxia across the LC remained consistent across all cases. Specifically, moderately

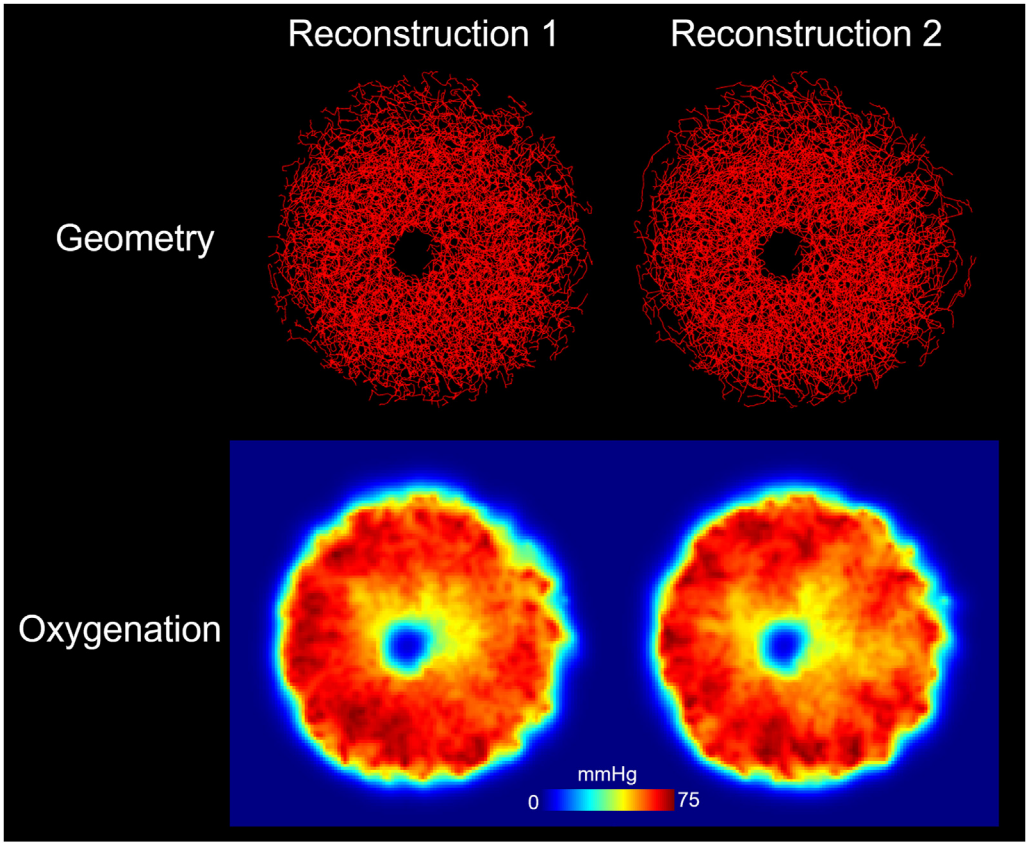

Figure 3. Two independent reconstructions from the same labeled eye. Both reconstructions exhibited similar geometry and oxygenation, indicating excellent repeatability in reconstruction.

elevated IOP caused mild hypoxia across a substantial portion of the LC, while severe hypoxia was limited to extreme IOP elevations. These findings highlight the robustness of our results under varying diameter assumptions.

Discussion

Our goal was to evaluate how LC oxygenation is affected by tissue distortions resulting from elevated IOP. Specifically, we used 3D eye-specific numerical models of the LC vasculature

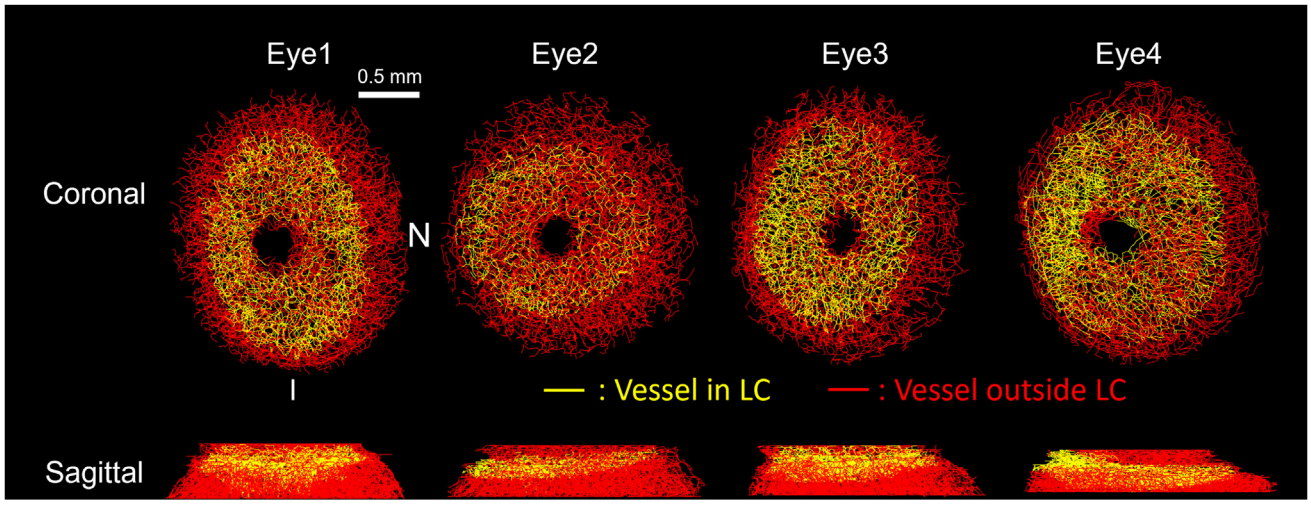

Figure 4. Reconstructed vasculatures of the ONH of the 4 eyes used in this work. All 4 networks were reconstructed from the right eyes (OD) of healthy monkeys. To improve boundary conditions, we simulated the full volumes shown, but the analyses focused on the LC region (segments colored in yellow). LC = lamina cribrosa; ONH = optic nerve head.

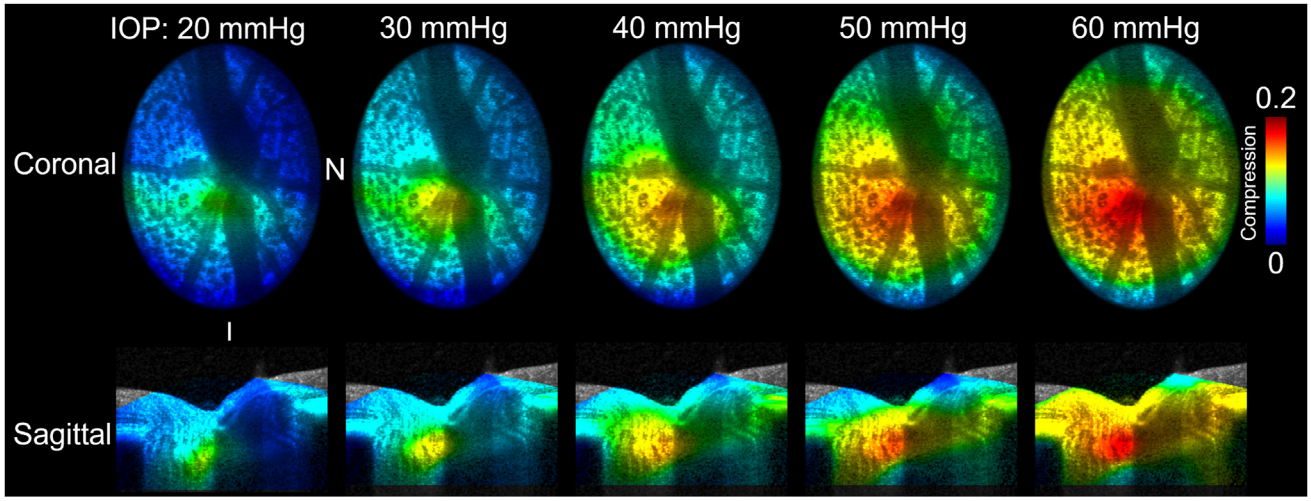

Figure 5. The ONH compression fields under various IOPs. The fields were derived using the DVC technique to quantify tissue deformation from OCT images acquired at the baseline (10 mmHg) and elevated IOPs. The magnitude of the compression increased with IOP. The coronal views of deformations are shown in OD configuration. Note that colors indicating compression are only shown where the compression was measured with the DVC. A DVC region was defined that completely enclosed the scleral canal region where the vasculature was modeled to ensure accurate compressions were computed everywhere necessary. DVC = digital volume correlation; IOP = intraocular pressure; OD = right eye; ONH = optic nerve head.

subjected to experimentally determined IOP-induced tissue deformations for several IOP levels from 10 mmHg to 60 mmHg. Digital volume correlation–determined tissue strain was mapped to vascular deformations using first a cross-sectional strain mapping technique and later an isotropic compression technique. We then used numerical simulations to determine LC hemodynamics in each case, and from these, the oxygenation throughout the LC, paying particular attention to measure the fraction of LC under mild or severe hypoxia. Three main findings arise from the models in this work. First, LC oxygenation was generally predicted to decrease as IOP increases. Second, moderately elevated IOP (20–30 mmHg) can lead to mild hypoxia in a substantial part (>20%) of the LC. Severe hypoxia region occurred for extreme IOP

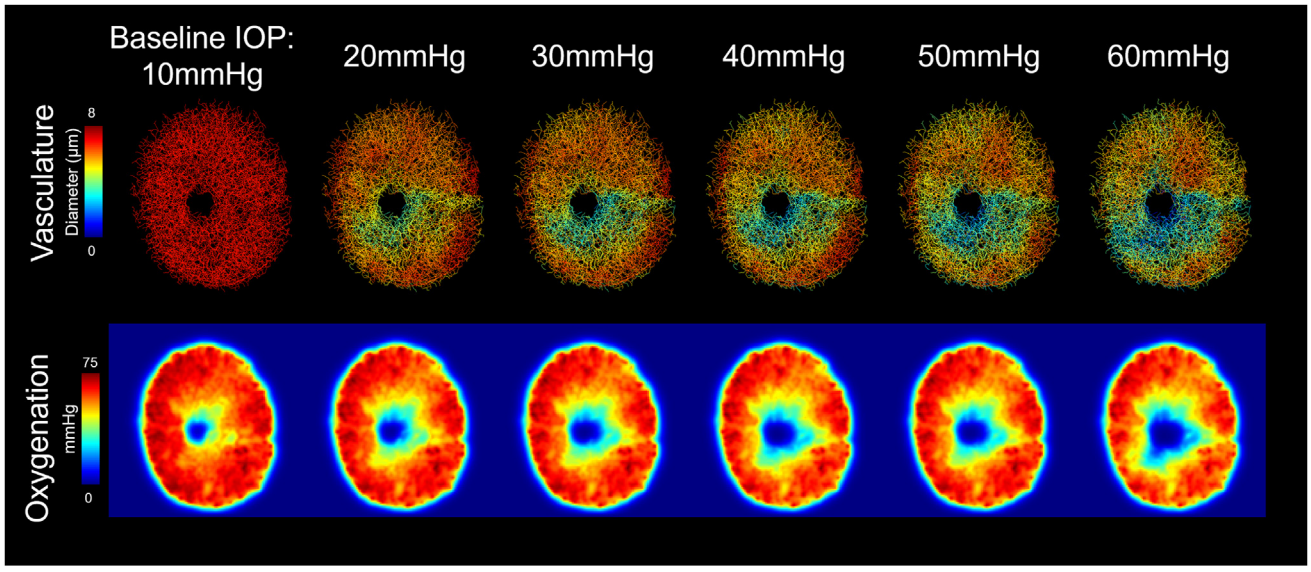

Figure 6. Eye 1 vasculature deformation and oxygenation at different IOPs for cross-sectional strain mapping. The diameters of the vasculature and the oxygenation decreased with IOP elevation. Regions of low oxygenation are primarily near the central portion of the ONH, although it appears to be more evenly split between the superior and inferior portions of the disc than one might assume given that the distortion and vessel compression seem concentrated in the inferior region. High IOP (>40 mmHg) caused a substantial region of vessel deformation (green and blue). As we mentioned in the Methods section, vessel would nearly fully collapse when its diameter reaches the RBC's size (~2 μm). Here, the vessel diameters never reach that value. Animation illustrating the changes in a small region of the ONH vasculature, including deformation, hemodynamics, and oxygenation, is presented in Videos 4 and 5. IOP = intraocular pressure; ONH = optic nerve head; RBC = red blood cell.

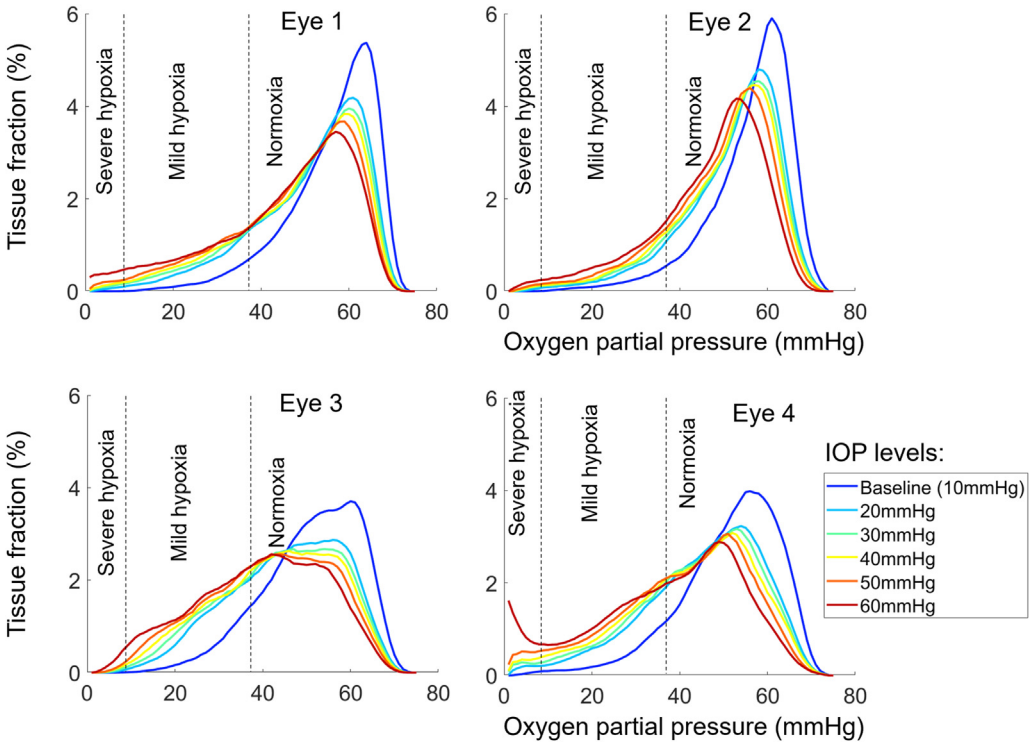

Figure 7. Lamina cribrosa oxygenation frequency distribution for the 4 eyes at 6 IOPs under the cross-sectional deformation mapping model. The oxygen frequency curves gradually shift to the left as IOP increases for all 4 eyes. This indicates an association between elevated IOP and decreased oxygenation within the LC. The most substantial change in LC oxygenation frequency is observed during the initial rise in IOP (baseline to 20 mmHg). On the other hand, even under high IOP, only a minimal proportion of tissue falls under severe hypoxia. IOP = intraocular pressure; LC = lamina cribrosa.

elevations (50−60 mmHg). Third, although IOP-induced deformations were roughly proportional to the level of IOP increase, the effects on LC oxygenation were larger at the initial increases in IOP, decreasing for higher IOPs. We subsequently discuss in detail each of these results, as well as the most important aspects of our modeling that readers should keep in mind when interpreting our results.

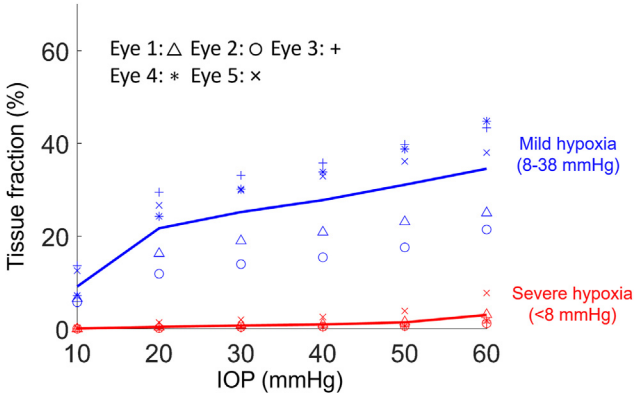

Figure 8. The relationship between IOP and hypoxia region in LC under a cross-sectional model. Results varied slightly between eyes, but overall, both the mild hypoxia and severe hypoxia regions increased as IOP increased. For moderate IOP elevation (20−30 mmHg), the mild hypoxia region increased significantly ($P < 0.05$). About 25% of LC tissue suffered from mild hypoxia when IOP reached 30 mmHg. Only few severe hypoxia regions (<5%) were observed under extremely high IOP (>50 mmHg). IOP = intraocular pressure; LC = lamina cribrosa.

LC Oxygenation Generally Decreased as IOP Increased

From baseline (10 mmHg) to extremely elevated IOP (60 mmHg), the oxygen distribution curve showed a general decreasing trend with IOP elevation. The hypoxic regions, both mild and severe, enlarged with IOP increases.

The association between LC oxygenation and IOP can be explained as follows. Qualitatively, the entire ONH is deformed during an IOP elevation. The fragile vessels within the ONH experience stretch, compression, and distortion. A deformed vasculature will then alter the LC microcirculation and potentially compromise the LC blood or oxygen supply. In this work, from a quantitative perspective, we found that even a small IOP-induced ONH deformation (e.g., ∼5% compression under 30 mmHg of IOP) leads to a substantial decrease in LC oxygenation (∼25% mild hypoxia). Our previous work[45] also showed that LC oxygenation is susceptible to IOP-induced deformation. This can be attributed to 2 main reasons. First, the capillaries are softer and more susceptible to deformations than the fiber-rich tissues in the LC.[43] The cross-sectional

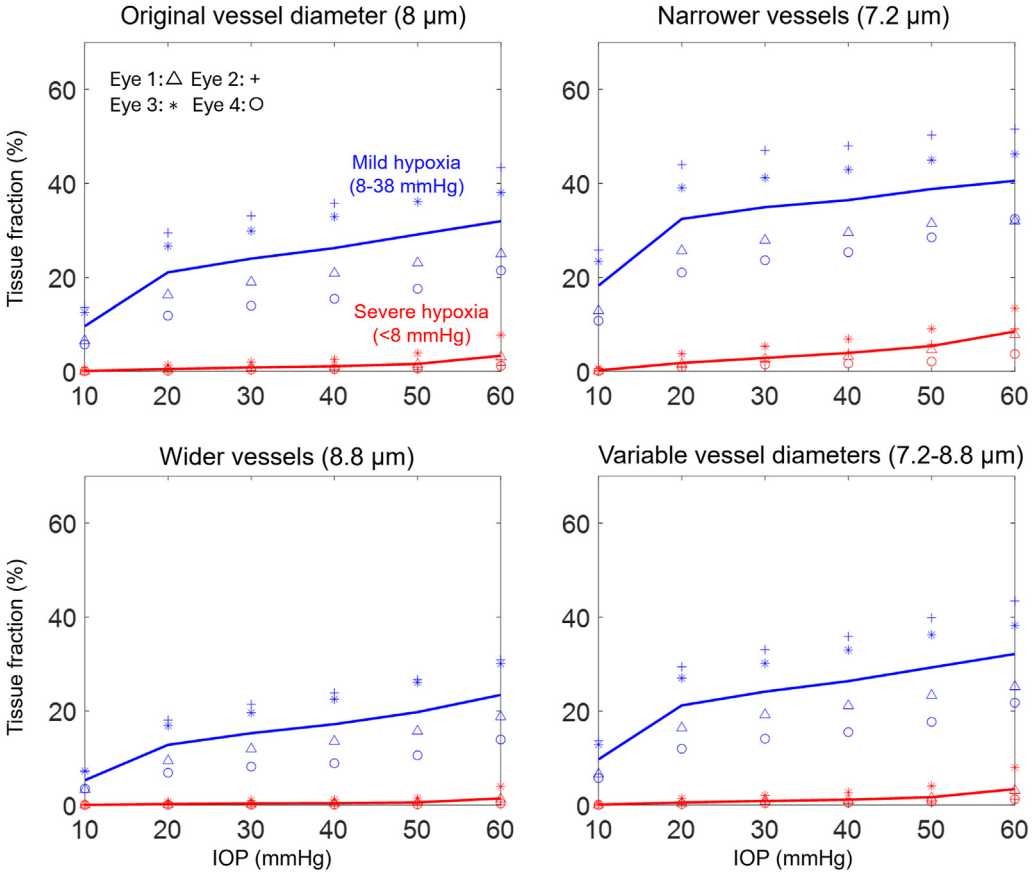

Figure 13. Relationship between IOP and hypoxia region in LC under different diameter settings. These are "baseline" diameters before IOP-induced distortions. Larger diameters resulted in higher oxygenation and fewer hypoxic regions. Across all cases, moderately elevated IOP caused mild hypoxia across a substantial portion of the LC, while severe hypoxia occurred only under extreme IOP elevations. IOP = intraocular pressure; LC = lamina cribrosa.

strain mapping model shows that the deformation of a capillary is approximately 3 times that of the surrounding tissue. Therefore, elevated IOP will induce a larger deformation on the LC vessels, leading to smaller diameters. Second, the flow conductance, defined by the ease with which blood can flow through a vessel, is sensitive to the vessel diameter, primarily from the quartic power relationship in Poiseuille law, and the diameter-dependent blood viscosity for RBCs.[47] These 2 effects amplify the influence of IOP on LC blood supply and, consequently, on LC oxygen supply.

Moderately elevated IOP (20−30 mmHg) can lead to mild hypoxia in a substantial part (>20%) of the LC. Some severe hypoxia regions occurred for extreme IOP elevations (50−60 mmHg). Intraocular pressure−induced ONH deformation increased with higher IOP levels, resulting in a significant expansion of the LC hypoxia region. Based on the physiological and pathological scenarios, mild hypoxia (<5% oxygen) and severe hypoxia (<1% oxygen) were selected as indicators to evaluate the potential damage from the elevated IOP on LC oxygenation.

Mild hypoxia is considered to occur at oxygenation levels that hypoxia responses start being detected.[55] Short-term mild hypoxia can be reversed by blood flow autoregulation.[59,60] However, if mild hypoxia is sustained chronically, it may contribute to neural tissue damage. Therefore, our models predict that long-term, moderately elevated IOP may lead to progressive and irreversible neural tissue effects, potentially resulting in or contributing to glaucoma.

Severe hypoxia can cause immediate and irreversible tissue damage. Individuals experiencing acutely elevated IOP are at risk of rapid vision loss and neural tissue damage.[61] This could be seen as a contradiction: only a few severe hypoxia regions (<5%) were observed under extremely high IOP, even though experimentally such a high IOP level will likely lead to widespread damage in a short time.[62] One potential explanation could be that the extremely high IOP could impact eye circulation and vision signaling other than in the lamina region. For example, an acute, extremely high IOP challenge can damage retinal circulation in closed-angle glaucoma.[61] We focus on the effects of milder, chronically elevated IOP on the LC region and therefore could underestimate the effects in extreme cases. Conversely, moderately elevated IOP typically does not lead to sudden vision loss or acute neural tissue damage. This is consistent with our findings that severe hypoxia does not occur in moderately elevated IOP.

It is worth noting that our results rely on the local vessel deformation mapping method. Because the actual vessel deformations resulting from IOP are still not known, we used 2 methods, cross-sectional strain mapping and isotropic compression mapping, as reasonable estimates. Although the trends were similar, the IOP effects were larger in the isotropic mapping case, with larger mild or severe hypoxia regions. Further experimental and modeling work is necessary to address the IOP effect on local vessel deformation and LC oxygenation.

Although IOP-induced deformations were roughly proportional to the level of IOP increase, the effects on LC oxygenation were larger at the initial increases in IOP, decreasing for higher IOPs. As IOP increased, ONH deformations became more pronounced. This deformation compromises the blood supply in ONH and results in reduced LC oxygenation. Interestingly, the most significant change in LC oxygenation occurred as IOP began to rise from 10 mmHg to 20 mmHg. This can be understood through the IOP-induced deformation and the compliance of the LC, defined as the ability of the LC to deform in response to pressure changes. Experimental observations have indicated that LC compliance exhibits a nonlinear behavior in response to elevated IOP.[63] When IOP experiences a moderate increase, the LC deforms more easily. This higher compliance at moderate IOP levels results in rapid and substantial deformation of the LC.

As IOP continues to rise beyond moderate levels, the LC becomes less compliant, and its deformation grows at a slower rate. This indicates that the LC stiffens with higher pressure, making it less capable of further deformation. This nonlinear compliance behavior explains why the most substantial reduction in LC oxygenation occurs during the early stages of IOP elevation.

Additionally, this finding is consistent with the crimp behavior of LC fibers. Crimping refers to the wavy pattern of collagen fibers in the LC. When subjected to moderate IOP increases, these crimped fibers can stretch and straighten, contributing to the initial higher compliance and significant deformation. As the fibers straighten out, the LC becomes less compliant, leading to a slower growth of deformation with further increases in IOP.[64]

This study integrates 3D eye-specific LC vascular networks with in vivo ONH deformation data. We further employed a biomechanical-based strain mapping approach to capture vessel deformations. This allowed us to perform a more realistic hemodynamic and oxygenation simulation for elevated IOP compared with highly simplified generic cases, thus providing a more precise evaluation of the IOP impact. Additionally, our work provides a systematic analysis of multiple eyes with low to high IOPs. The use of multiple eye-specific vascular networks reduced the influence of individual variances, enhancing the robustness of our findings.

It is important to consider the limitations of this study. A limitation of this work is that the maps of IOP-related tissue deformation were obtained from different eyes than those used for vessel reconstructions, requiring alignment techniques to match them. It is unclear how this may have influenced the results. Although the oxygen profile was slightly different among different vessel networks, the overall trend of the tissue hypoxia fraction was consistent for the 4-vessel networks. This suggests that the details of the vessel network do not undermine our findings.

Another limitation is that our work only considers the static status of LC hemodynamics and oxygenation. However, in vivo blood or oxygen supply involved various regulation mechanisms to meet the changing demand of organisms. Short-term blood flow autoregulation has been identified as a significant factor in hemodynamics and oxygenation for the eye.[35,36,60,65] Long-term vessel remodeling in the LC was also observed in the development of glaucoma.[5,66] Although the precise regulation and remodeling in LC remain unknown, we acknowledge that they could alter the LC blood and oxygen supply.[60,65,67–70] Future research should incorporate the dynamic aspects of the LC blood and oxygen supply, which could contribute to the development of some pathological scenarios, such as glaucoma.

We employed cross-sectional strain mapping methods. While we considered the luminal vessels embedded within the tissue, our approach simplified the model by assuming the vessel wall and the fiber-rich LC tissue as homogeneous linear elastic materials. This simplification serves 2 primary purposes: Firstly, it helps to reduce the computational cost of the coupled system. Secondly, it avoids the need for certain parameters in a more complex nonlinear model, which is hard to measure in experiments. Based on the homogeneous linear assumption, our method may underestimate or overestimate the vessel compressions in the large deformation case. More advanced methods to incorporate the local mechanical properties of the LC into the predictions of vessel distortion will likely have to take into account whether a specific vessel segment is within a collagen beam or not.[71]

Our model primarily focuses on cross-sectional deformation rather than axial deformations, such as bending or distortion. This is because flow resistance is highly sensitive to vessel diameters—proportional to the fourth power in Poiseuille flow—and even more when considering the Fåhræus–Lindqvist effect. In contrast, resistance is only linearly proportional to vessel length, which exhibits minimal change in our case (<10%). While vessel distortions might affect RBC rheology in very-small-diameter and highly tortuous vessels, such effects are not included in the current model and will be explored in future studies with advanced experimental measurements.

Our simulation model and algorithm have been published and validated for general vascular systems. However, specific parameters required for ONH models, such as oxygen consumption rates, blood flow boundary conditions, and in vivo vessel diameters, are not yet available from experimental measurements. We conducted parametric analyses to evaluate the potential effects of these parameters on the results. Techniques with higher signal penetration, like ultrasound[72] and magnetic resonance imaging, are able to provide estimates of blood flow, but the small size of the eye is still a challenge. For oxygenation, techniques like visible light OCT[27] for oxygen saturation assessment and metabolic markers for identifying hypoxic tissues have been explored. Future work will aim to integrate our

modeling framework with these advanced experimental techniques to achieve more accurate in vivo assessments of ONH hemodynamics and oxygenation.

As noted in the Results, some vessels exhibited non-monotonic changes in diameter with IOP increases (Fig S9). The mechanisms underlying this observation remain unknown. Some possible causes include fluctuations in the heartbeat cycle at the moment the vessels were imaged,[73] actions by the ONH autoregulatory mechanism, or they could be approximations and inaccuracies in the strain analysis of the noisy OCT images.

In summary, we analyzed the LC oxygenation under various elevated IOP cases. Moderately elevated IOP can lead to mild hypoxia in a substantial part of the LC, which, if sustained chronically, may contribute to neural tissue damage. For extreme IOP elevations, severe hypoxia was predicted, potentially causing more immediate damage. The findings provide a systematic picture of the IOP-induced deformation effect on the LC, including multiple LC vascular networks, 2 strain mapping techniques, and ONH deformation under various IOPs. This is important to help understand ONH physiology and pathology.

Footnotes and Disclosures

Originally received: August 22, 2024.
Final revision: January 6, 2025.
Accepted: January 27, 2025.
Available online: January 31, 2025. Manuscript no. XOPS-D-24-00317.

[1] Department of Ophthalmology, University of Pittsburgh, Pittsburgh, Pennsylvania.

[2] Department of Biomedical Engineering, University of Mississippi, University, Mississippi.

[3] Department of Mechanical Engineering, University of Mississippi, University, Mississippi.

[4] Department of Bioengineering, University of Pittsburgh, Pittsburgh, Pennsylvania.

Disclosures:

All authors have completed and submitted the ICMJE disclosures form.

The author(s) have no proprietary or commercial interest in any materials discussed in this article.

This study was supported by the National Institutes of Health (R01-EY023966, R01-EY031708, R01-HD083383, P30-EY008098, T32-EY017271); the Eye & Ear Foundation of Pittsburgh; Research to Prevent Blindness (unrestricted grant to UPMC Ophthalmology and Stein Innovation Award to I.A.S.); and the BrightFocus Foundation (postdoctoral award to Y.H.).

HUMAN SUBJECTS: No human subjects were included in this study.

ANIMAL SUBJECTS: Animal subjects were used in this study. All procedures were approved by the University of Pittsburgh's Institutional Animal Care and Use Committee and adhered to both the guidelines set forth in the National Institute of Health's Guide for the Care and Use of Laboratory Animals and the Association for Research in Vision and Ophthalmology statement for the use of animals in ophthalmic and vision research.

Author Contributions:

Conception and design: Lu, Hua, Sigal

Data collection: Wang, Zhong, Theophanous, Tahir

Analysis and interpretation: Lu, Wang, Tian, Lee, Sigal

Obtained funding: Sigal

Overall responsibility: Lu, Sigal

Abbreviations and Acronyms:
IOP = intraocular pressure; **LC** = lamina cribrosa; **ONH** = optic nerve head; **PO_2** = oxygen partial pressure; **RBC** = red blood cell; **3D** = 3-dimensional.

Keywords:
Lamina cribrosa, Oxygenation, Hemodynamic, Intraocular pressure, Hypoxia.

Correspondence:
Ian A. Sigal, PhD, Laboratory of Ocular Biomechanics, Department of Ophthalmology, University of Pittsburgh Medical Center, UPMC Mercy Pavilion, 1622 Locust St. Rm. 7.382, Pittsburgh, PA 15219. E-mail: ian.sigal@gmail.com.

References

1. Quigley H, Anderson DR. The dynamics and location of axonal transport blockade by acute intraocular pressure elevation in primate optic nerve. *Invest Ophthalmol Vis Sci*. 1976;15:606–616.
2. Nickells RW. The cell and molecular biology of glaucoma: mechanisms of retinal ganglion cell death. *Invest Ophthalmol Vis Sci*. 2012;53:2476–2481.
3. Howell GR, Libby RT, Jakobs TC, et al. Axons of retinal ganglion cells are insulted in the optic nerve early in DBA/2J glaucoma. *J Cell Biol*. 2007;179:1523–1537.
4. Quigley H. *Glaucoma Lancet*. 2011;377:1367–1377.
5. Quigley HA, Nickells RW, Kerrigan LA, et al. Retinal ganglion cell death in experimental glaucoma and after axotomy occurs by apoptosis. *Invest Ophthalmol Vis Sci*. 1995;36:774–786.
6. Pitha I, Du L, Nguyen T, Quigley H. IOP and glaucoma damage: the essential role of optic nerve head and retinal mechanosensors. *Prog Retin Eye Res*. 2023;99:101232.
7. Stowell C, Burgoyne CF, Tamm ER, et al. Biomechanical aspects of axonal damage in glaucoma: a brief review. *Exp Eye Res*. 2017;157:13–19.
8. Burgoyne CF, Downs JC, Bellezza AJ, et al. The optic nerve head as a biomechanical structure: a new paradigm for understanding the role of IOP-related stress and strain in the pathophysiology of glaucomatous optic nerve head damage. *Prog Retin Eye Res*. 2005;24:39–73.
9. Chuangsuwanich T, Birgersson KE, Thiery A, et al. Factors influencing lamina cribrosa microcapillary hemodynamics and oxygen concentrations. *Invest Ophthalmol Vis Sci*. 2016;57:6167–6179.
10. Chuangsuwanich T, Hung PT, Wang X, et al. Morphometric, hemodynamic, and biomechanical factors influencing blood flow and oxygen concentration in the human lamina cribrosa. *Invest Ophthalmol Vis Sci*. 2020;61:3.

11. Sigal IA. Interactions between geometry and mechanical properties on the optic nerve head. *Invest Ophthalmol Vis Sci*. 2009;50:2785–2795.
12. Sigal IA, Grimm JL. A few good responses: which mechanical effects of IOP on the ONH to study? *Invest Ophthalmol Vis Sci*. 2012;53:4270–4278.
13. Voorhees AP, Hua Y, Brazile BL, et al. So-called lamina cribrosa defects may mitigate IOP-induced neural tissue insult. *Invest Ophthalmol Vis Sci*. 2020;61:15.
14. Zhang L, Albon J, Jones H, et al. Collagen microstructural factors influencing optic nerve head biomechanics. *Invest Ophthalmol Vis Sci*. 2015;56:2031–2042.
15. Brooks D, Samuelson D, Gelatt K. Ultrastructural changes in laminar optic nerve capillaries of beagles with primary open-angle glaucoma. *Am J Vet Res*. 1989;50:929–935.
16. Fechtner RD, Weinreb RN. Mechanisms of optic nerve damage in primary open angle glaucoma. *Surv Ophthalmol*. 1994;39:23–42.
17. Quigley HA, McKinnon SJ, Zack DJ, et al. Retrograde axonal transport of BDNF in retinal ganglion cells is blocked by acute IOP elevation in rats. *Invest Ophthalmol Vis Sci*. 2000;41:3460–3466.
18. Carichino L, Guidoboni G, Arieli Y, et al. Effect of lamina cribrosa deformation on the hemodynamics of the central retinal artery: a mathematical model. *Invest Ophthalmol Vis Sci*. 2012;53:2836.
19. Geijer C, Bill A. Effects of raised intraocular pressure on retinal, prelaminar, laminar, and retrolaminar optic nerve blood flow in monkeys. *Invest Ophthalmol Vis Sci*. 1979;18:1030–1042.
20. Beach J, Ning J, Khoobehi B. Oxygen saturation in optic nerve head structures by hyperspectral image analysis. *Curr Eye Res*. 2007;32:161–170.
21. Carreau A, Hafny-Rahbi BE, Matejuk A, et al. Why is the partial oxygen pressure of human tissues a crucial parameter? Small molecules and hypoxia. *J Cell Mole Med*. 2011;15:1239–1253.
22. Ferrez P, Chamot S, Petrig B, et al. Effect of visual stimulation on blood oxygenation in the optic nerve head of miniature pigs: a pilot study. *Klin Monbl Augenheilkd*. 2004;221:364–366.
23. Ortiz-Prado E, Dunn JF, Vasconez J, et al. Partial pressure of oxygen in the human body: a general review. *Am J Blood Res*. 2019;9:1.
24. Mari JM, Strouthidis NG, Park SC, Girard MJ. Enhancement of lamina cribrosa visibility in optical coherence tomography images using adaptive compensation. *Invest Ophthalmol Vis Sci*. 2013;54:2238–2247.
25. Lee EJ, Han DK, Roh YJ, Kim T-W. Underlying microstructure of the lamina cribrosa at the site of microvasculature dropout. *Invest Ophthalmol Vis Sci*. 2024;65:47.
26. Numa S, Akagi T, Uji A, et al. Visualization of the lamina cribrosa microvasculature in normal and glaucomatous eyes: a swept-source optical coherence tomography angiography study. *J Glaucoma*. 2018;27:1032–1035.
27. Pi S, Hormel TT, Wei X, et al. Retinal capillary oximetry with visible light optical coherence tomography. *Proc Natl Acad Sci U S A*. 2020;117:11658–11666.
28. Rao HL, Pradhan ZS, Weinreb RN, et al. A comparison of the diagnostic ability of vessel density and structural measurements of optical coherence tomography in primary open angle glaucoma. *PloS One*. 2017;12:e0173930.
29. Qian X, Kang H, Li R, et al. In vivo visualization of eye vasculature using super-resolution ultrasound microvessel imaging. *IEEE Trans Biomed Eng*. 2020;67:2870–2880.
30. Li Y, Cheng H, Duong TQ. Blood-flow magnetic resonance imaging of the retina. *Neuroimage*. 2008;39:1744–1751.
31. Causin P, Guidoboni G, Malgaroli F, et al. Blood flow mechanics and oxygen transport and delivery in the retinal microcirculation: multiscale mathematical modeling and numerical simulation. *Biomech Model Mechanobiol*. 2016;15:525–542.
32. Hua Y, Lu Y, Walker J, et al. Eye-specific 3D modeling of factors influencing oxygen concentration in the lamina cribrosa. *Exp Eye Res*. 2022;220:109105.
33. Causin P, Guidoboni G, Harris A, et al. A poroelastic model for the perfusion of the lamina cribrosa in the optic nerve head. *Math Biosci*. 2014;257:33–41.
34. Walker JA, Hua Y, McDonald H, et al. Factors influencing oxygen concentration in the lamina cribrosa. *Invest Ophthalmol Vis Sci*. 2020;61:632.
35. Sala L, Prud'Homme C, Guidoboni G, et al. The ocular mathematical virtual simulator: a validated multiscale model for hemodynamics and biomechanics in the human eye. *Int J Numer Method Biomed Eng*. 2024;40(2):e3791.
36. Guidoboni G, Harris A, Cassani S, et al. Intraocular pressure, blood pressure, and retinal blood flow autoregulation: a mathematical model to clarify their relationship and clinical relevance. *Invest Ophthalmol Vis Sci*. 2014;55:4105–4118.
37. Lee P-Y, Hua Y, Brazile BL, et al. A workflow for three-dimensional reconstruction and quantification of the monkey optic nerve head vascular network. *J Biomech Eng*. 2022;144:061006.
38. Campbell IC, Coudrillier B, Mensah J, et al. Automated segmentation of the lamina cribrosa using Frangi's filter: a novel approach for rapid identification of tissue volume fraction and beam orientation in a trabeculated structure in the eye. *J R Soc Interface*. 2015;12:20141009.
39. Zhong F, Wang B, Wei J, et al. A high-accuracy and high-efficiency digital volume correlation method to characterize in-vivo optic nerve head biomechanics from optical coherence tomography. *Acta Biomater*. 2022;143:72–86.
40. Hayreh SS. Blood supply of the optic nerve head and its role in optic atrophy, glaucoma, and oedema of the optic disc. *Br J Ophthalmol*. 1969;53:721.
41. Tran H, Jan N-J, Hu D, et al. Formalin fixation and cryosectioning cause only minimal changes in shape or size of ocular tissues. *Sci Rep*. 2017;7:1–11.
42. An D, Pulford R, Morgan WH, et al. Associations between capillary diameter, capillary density, and microaneurysms in diabetic retinopathy: a high-resolution confocal microscopy study. *Transl Vis Sci Technol*. 2021;10:6.
43. Camasão D, Mantovani D. The mechanical characterization of blood vessels and their substitutes in the continuous quest for physiological-relevant performances. A critical review. *Mater Today Bio*. 2021;10:100106.
44. Shilo M, Gefen A. Identification of capillary blood pressure levels at which capillary collapse is likely in a tissue subjected to large compressive and shear deformations. *Comput Methods Biomech Biomed Engin*. 2012;15:59–71.
45. Lu Y, Hua Y, Wang B, et al. The robust lamina cribrosa vasculature: perfusion and oxygenation under elevated intraocular pressure. *Invest Ophthalmol Vis Sci*. 2024;65:1.
46. Pries AR, Secomb TW. Microvascular blood viscosity in vivo and the endothelial surface layer. *Am J Physiol Heart Circ Physiol*. 2005;289(6):H2657–H2664.

47. Pries AR, Secomb TW. *Blood flow in microvascular networks. Microcirculation*. Cambridge, MA: Academic Press; 2008:3−36.
48. Ebrahimi S, Bagchi P. A computational study of red blood cell deformability effect on hemodynamic alteration in capillary vessel networks. *Sci Rep*. 2022;12:4304.
49. Williams J, Turney B, Moulton D, Waters S. Effects of geometry on resistance in elliptical pipe flows. *J Fluid Mech*. 2020;891:A4.
50. Popel AS. Theory of oxygen transport to tissue. *Crit Rev Biomed Eng*. 1989;17:257.
51. Secomb TW, Hsu R, Park EY, Dewhirst MW. Green's function methods for analysis of oxygen delivery to tissue by microvascular networks. *Ann Biomed Eng*. 2004;32:1519−1529.
52. Lu Y, Hu D, Ying W. A fast numerical method for oxygen supply in tissue with complex blood vessel network. *PloS one*. 2021;16:e0247641.
53. Leach R, Treacher D. Oxygen transport2. Tissue hypoxia. *BMJ*. 1998;317:1370−1373.
54. Loiacono LA, Shapiro DS. Detection of hypoxia at the cellular level. *Crit Care Clin*. 2010;26:409−421.
55. McKeown S. Defining normoxia, physoxia and hypoxia in tumours—implications for treatment response. *Br J Radiol*. 2014;87:20130676.
56. Selbach MJ, Wonka F, Hoper J, Funk RH. Effects of elevated intraocular pressure on haemoglobin oxygenation in the rabbit optic nerve head: a microendoscopical study. *Exp Eye Res*. 1999;69:301−309.
57. Hockel M, Vaupel P. Tumor hypoxia: definitions and current clinical, biologic, and molecular aspects. *J Natl Cancer Inst*. 2001;93:266−276.
58. Ortiz-Prado E, Natah S, Srinivasan S, Dunn JF. A method for measuring brain partial pressure of oxygen in unanesthetized unrestrained subjects: the effect of acute and chronic hypoxia on brain tissue PO2. *J Neurosci Method*. 2010;193:217−225.
59. Harris A, Ciulla TA, Chung HS, Martin B. Regulation of retinal and optic nerve blood flow. *Arch Ophthalmol*. 1998;116:1491−1495.
60. Wang L, Burgoyne CF, Cull G, et al. Static blood flow autoregulation in the optic nerve head in normal and experimental glaucoma. *Invest Ophthalmol Vis Sci*. 2014;55:873−880.
61. Sun X, Dai Y, Chen Y, et al. Primary angle closure glaucoma: what we know and what we don't know. *Prog Retin Eye Res*. 2017;57:26−45.
62. Xuan M, Wang W, Bulloch G, et al. Impact of acute ocular hypertension on retinal ganglion cell loss in mice. *Transl Vis Sci Technol*. 2024;13:17.
63. Tun TA, Thakku SG, Png O, et al. Shape changes of the anterior lamina cribrosa in normal, ocular hypertensive, and glaucomatous eyes following acute intraocular pressure elevation. *Invest Ophthalmol Vis Sci*. 2016;57:4869−4877.
64. Foong TY, Hua Y, Amini R, Sigal IA. Who bears the load? IOP-induced collagen fiber recruitment over the corneoscleral shell. *Expe Eye Res*. 2023;230:109446.
65. Yu J, Liang Y, Thompson S, et al. Parametric transfer function analysis and modeling of blood flow autoregulation in the optic nerve head. *Int J Physiol Pathophysiol Pharmacol*. 2014;6:13.
66. Hayreh S. The optic nerve head circulation in health and disease. *Ophthalmic Lit*. 1996;2:111.
67. Hayreh SS. Blood flow in the optic nerve head and factors that may influence it. *Prog Retin Eye Res*. 2001;20:595−624.
68. Mackenzie PJ, Cioffi GA. Vascular anatomy of the optic nerve head. *Can J Ophthalmol*. 2008;43:308−312.
69. Mozaffarieh M, Grieshaber MC, Flammer J. Oxygen and blood flow: players in the pathogenesis of glaucoma. *Mole Vis*. 2008;14:224.
70. Orgül S, Gugleta K, Flammer J. Physiology of perfusion as it relates to the optic nerve head. *Surv Ophthalmol*. 1999;43:S17−S26.
71. Waxman S, Brazile BL, Yang B, et al. Lamina cribrosa vessel and collagen beam networks are distinct. *Exp Eye Re*. 2022;215:108916.
72. Ul BH, Mitchell B, Chen S, Palko J. Super-Resolution ultrasound localization microscopy using high-frequency ultrasound to measure ocular perfusion velocity in the rat eye. *Bioengineering*. 2023;10:689.
73. Solano MM, Richer E, Cheriet F, et al. Mapping pulsatile optic nerve head deformation using OCT. *Ophthalmol Sci*. 2022;2:100205.